



HAL
open science

Iron (oxy)hydroxide and hematite micro- to nano-inclusions in diagenetic dolomite from a 2.4 Ga banded iron formation (Minas Gerais, Brazil)

Beate Orberger, Christiane Wagner-Raffin Wagner, Alina Tudryn, Benoît Baptiste, Richard Wirth, Rachael Morgan, Serge Miska

► To cite this version:

Beate Orberger, Christiane Wagner-Raffin Wagner, Alina Tudryn, Benoît Baptiste, Richard Wirth, et al.. Iron (oxy)hydroxide and hematite micro- to nano-inclusions in diagenetic dolomite from a 2.4 Ga banded iron formation (Minas Gerais, Brazil). *European Journal of Mineralogy*, 2017, 29, pp.971 - 983. 10.1127/ejm/2017/0029-2679 . hal-03822820

HAL Id: hal-03822820

<https://hal.science/hal-03822820v1>

Submitted on 20 Oct 2022

HAL is a multi-disciplinary open access archive for the deposit and dissemination of scientific research documents, whether they are published or not. The documents may come from teaching and research institutions in France or abroad, or from public or private research centers.

L'archive ouverte pluridisciplinaire **HAL**, est destinée au dépôt et à la diffusion de documents scientifiques de niveau recherche, publiés ou non, émanant des établissements d'enseignement et de recherche français ou étrangers, des laboratoires publics ou privés.

Iron (oxy)hydroxide and hematite micro- to nano-inclusions in diagenetic dolomite from a 2.4 Ga banded iron formation (Minas Gerais, Brazil)

BEATE ORBERGER^{1,*}, CHRISTIANE WAGNER², ALINA TUDRYN¹, BENOÎT BAPTISTE³, RICHARD WIRTH⁴,
RACHAEL MORGAN¹ and SERGE MISKA¹

¹ GEOPS, UMR 8148, Univ. Paris-Sud, CNRS, Université Paris-Saclay, rue du Belvédère, Bât. 504-509,
91405 Orsay, France

*Corresponding author, e-mail: beate.orberger@u-psud.fr

² Sorbonne Universités, UPMC, Univ Paris 06, CNRS, Institut des Sciences de la Terre de Paris (ISTeP),
4 place Jussieu, 75005 Paris, France

³ Sorbonne Universités, UPMC, Univ Paris 06, CNRS, IMPMC, 4 place Jussieu, 75005 Paris, France

⁴ Helmholtz Centre Potsdam, GFZ German Research Centre for Geosciences, Section 3.3,
Telegrafenberg, 14473 Potsdam, Germany

Abstract: The low-grade carbonate banded iron formation of the Aguas Claras mine, from the transition of the Caûe to the Gandarela Formation (2.4 Ga, Itabira Group, Brazil), is composed of porous and microsparitic dolomite, quartz, iron oxides and (oxy)hydroxides. Iron oxides occur as bands, veins and as inclusions in the dolomite crystals, whereas iron (oxy)hydroxides only occur as inclusions. Combined mineralogical analyses (X-ray diffraction, Raman spectroscopy, focused-ion-beam thinning and transmission electron microscopy) identified the inclusions in porous dolomite as hematite and minor goethite and/or ferrihydrite, whereas microsparitic dolomite only hosts hematite. Curie balance analysis on whole rock reveals that, at temperatures between ~680 °C and ~900 °C, hematite and iron (oxy)hydroxide inclusions react with the surrounding dolomite resulting in the assemblage: magnesioferrite (MgFe₂O₄), srebrodolskite (Ca₂Fe₂O₅), lime (CaO), portlandite (Ca(OH)₂) and periclase (MgO), whereas hematite and pure dolomite do so only at ~900 °C. This difference is an indirect argument for the presence of iron hydroxide inclusions within the dolomite. The inclusions are either single crystals or form clusters in pores. The fast-Fourier-transform diffraction pattern of one single crystal can be indexed as goethite and ferrihydrite. This finding suggests an incipient solid-state transformation of ferrihydrite to goethite rather than a dissolution-precipitation process. It is suggested that the clustered hematite and the goethite/ferrihydrite precipitated from Fe- and Si-bearing fluid inclusions, which were trapped during early diagenesis at about 2.4 Ga under oxygenated conditions. Microstructural evidence (e.g. dislocations in dolomite from hematite inclusions) point to maximum $T < 420$ °C. The preservation of goethite/ferrihydrite clustered inclusions during this low-temperature event may be due to their silica contents increasing their stability.

Key-words: goethite; hematite; iron ore; FIB TEM; Curie balance; magnetic hysteresis; X-ray diffraction; Raman spectroscopy; banded iron formation; Brazil; Minas Gerais.

1. Introduction

Banded iron formations (BIF) are comprised of complex textures and mineralogy resulting from fluid-rock interactions related to diagenesis, hydrothermalism, metamorphism and supergene alteration (e.g. Morris, 1985; Dalstra & Guedes, 2004; Klein, 2005; Beukes & Gutzmer, 2008; Angerer *et al.*, 2012; Orberger *et al.*, 2012, 2014; Morgan *et al.*, 2013). In general, most BIF types host hematite, magnetite and goethite as iron oxide or (oxy)hydroxide phases (e.g. Morris, 1980, 1985; Rosière *et al.*, 2008; Spier *et al.*, 2008; Orberger *et al.*, 2012; Morgan *et al.*, 2013). The precursor for hematite ores is proposed to be magnetite or siderite (e.g. Beukes & Gutzmer, 2008). These primary iron-bearing phases, carbonates and quartz

most likely precipitated from a mixture of hydrothermal fluids and seawater, sometimes with organic mediation (e.g. Isley, 1995; Bolhar *et al.*, 2004; Beukes & Gutzmer, 2008; Morgan *et al.*, 2013; Hashizume *et al.*, 2016). The primary minerals have undergone transformations since their deposition (between about 3.8 and 1.8 Ga), which have upgraded parts of the BIF into one of the world's largest source of iron ore (e.g. Spier *et al.*, 2007).

In modern seafloor hydrothermal environments, iron hydroxides (e.g. ferrihydrite) precipitate as primary minerals (e.g. Gloter *et al.*, 2004), which may evolve into spherulitic hematite during diagenesis as observed in the Red Sea (Taitel-Goldman & Singer, 2002). Even if iron hydroxides are the precursor to hematite in BIF, it is unlikely that these hydrous phases survived hydrothermal and metamorphic events after deposition (Morris, 1998).

At present, all iron hydroxides in BIF are attributed to ancient or modern supergene alteration (*e.g.* Morris, 1985, 1998; Beukes & Gutzmer, 2008; Spier *et al.*, 2008; Orberger *et al.*, 2012, 2014).

There are two main difficulties in retracing the origin of iron (oxy)hydroxides in BIF: (1) samples with early diagenetic signatures are rare, and (2) the poorly crystalline state and nano grain size of the iron oxides and (oxy)hydroxides may hinder unambiguous characterisation (*e.g.* Manceau & Drits, 1993; Cornell & Schwertmann, 2003; Gloter *et al.*, 2004). Previous petrological and mineralogical investigations by Morgan *et al.* (2013) and Pimenta da Silva *et al.* (2011) inferred a diagenetic origin for the low-grade carbonate BIF forming the transition of the 2.4 Ga Caûe Formation to the Gandarela Formation (Itabira Group, Minas Supergroup, Brazil; Babinski *et al.*, 1991, 1993; Spier *et al.*, 2008; Morgan *et al.*, 2013). These carbonate BIF are considered the protore of the high-grade iron ore of the Quadrilátero Ferrífero (QF; Dalstra & Guedes, 2004). Morgan *et al.* (2013) described numerous iron-bearing inclusions in dolomite of the low-grade diagenetic carbonate BIF.

In this paper, we present the first full characterisation of these iron-bearing inclusions by micro- and nano-scale methods: optical microscopy, scanning electron microscopy (SEM), focussed ion beam transmission electron microscopy (FIB-TEM), Raman spectroscopy and X-ray diffraction (XRD). These analyses were coupled with Curie balance, magnetic hysteresis and XRD measurements of the dolomite bands before and after decarbonation. This study allows retracing the origin of the iron oxides and hydroxides in the 2.4 Ga BIFs and contributes to the understanding of the transformation of ferrihydrite to goethite and their stability during low-temperature deformation.

2. Geological setting and sample material

The studied rock comes from a drill core at 51.6 m depth (PZ-INA55, Aguas Claras Mine, N22935532, E615556), sampling the carbonate-rich BIF at the transition of the Caûe Formation to the Gandarela Formation in the northern part of the QF (Fig. 1A and B). These formations belong to the Itabira Group (Minas Supergroup; Chemale *et al.*, 1994; Spier *et al.*, 2007; Rosière *et al.*, 2008; Fig. 1B). The QF was affected by two major orogenic events: (1) the Palaeoproterozoic Transamazonian/Mineiro (2.1–2.0 Ga) followed by intrusion of plutons and mafic dykes (1.9–1.8 Ga; Teixeira & Figueiredo, 1991; Chemale *et al.*, 1994); (2) the Neoproterozoic to Early Palaeozoic Brasiliano/Pan African Orogeny (0.65–0.50 Ga) occurring after the Post-Transamazonian rifting and basin formation (Alkim & Marshak, 1998). All these events result in synclines forming a dome-and-keel province, and in different degrees of metamorphism, which is expressed in the northern part of the QF as greenschist facies (Chemale *et al.*, 1994). The studied samples were selected from the part of the QF that is characterised by a very low metamorphic grade having even preserved diagenetic dolomite.

The Caûe Formation consists of alternating quartzitic and dolomitic BIF, and minor dolomite and shales. The Caûe Formation grades vertically and horizontally into the carbonate-rich Gandarela Formation (Spier *et al.*, 2007, 2008) but the transition is still not well defined (Dorr, 1969; Pimenta da Silva *et al.*, 2011). The latter authors considered this transition as stratigraphically continuous, rather than a later hydrothermally overprinted zone. Petrographic and rare earth-element studies on samples from this transition argue for a diagenetic origin of dolomite, having initially precipitated with quartz and iron oxyhydroxides from a mixture of hydrothermal fluids and sea water in a vent environment (Morgan *et al.*, 2013).

Seven samples from the Aguas Claras low-grade carbonate BIF drill core were studied by Morgan *et al.* (2013). One sample representing the less deformed BIF of this drill core was studied here. The whole-rock composition of this sample is (in wt%): total iron 26.71 (expressed as Fe₂O₃), FeO 0.42, SiO₂ 0.2, MnO 0.32, MgO 15.46, CaO 22.32, P₂O₅ 0.09, Al₂O₃ < 0.05, H₂O 0.15 and CO₂ 34.08 (Morgan *et al.*, 2013).

The BIF sample shows alternating pink and dark grey millimetric bands of bright rose coloured dolomite, quartz and massive grey iron oxides – mainly hematite (Fig. 2A). The microbanding is truncated by lenses composed of microsparitic dolomite or micrometric quartz (Fig. 2A). Micrometric veins of dolomite, parallel to banding and crosscutting the banding, and veins of hematite parallel to banding also occur (Fig. 2A and B). The red/pink dolomite bands are predominantly composed of porous and microsparitic dolomite (Fig. 2C), minor quartz and large hematite aggregates (Fig. 2D). The porous dolomite grains include abundant micro- and nanometric iron-bearing inclusions (Fig. 2D and E). Minor minerals interstitial to dolomite and quartz are apatite and chlorite.

Details on the mineral chemistry are given by Morgan *et al.* (2013), who did not distinguish between porous and microsparitic dolomite. In this study, the dolomite major-element composition (EMPA) varies from 28.3 to 31.4 wt% CaO, 20.3 to 22.2 wt% MgO and 0.2 to 1.8 wt% MnO. Iron content is highly variable (0.02–7 wt%), from grain to grain and within a single grain, which is most likely due to nanometric Fe-bearing inclusions within the dolomite crystals. However, it cannot be excluded that low Fe contents belong to a FeCO₃ component in the dolomite. This issue is discussed below.

3. Analytical methods

3.1. Electron microscopy (SEM and FIB-TEM)

Scanning electron microscopy (SEM) in back-scattered mode (BSE) was performed on polished thin sections. Two dolomite bands were selected for focused-ion-beam thinning (FIB) and analysis by transmission electron microscopy (TEM) (Fig. 2A, areas 1 and 2). Six FIB-foils (15 × 10 μm²) of 0.15 μm thickness were cut through

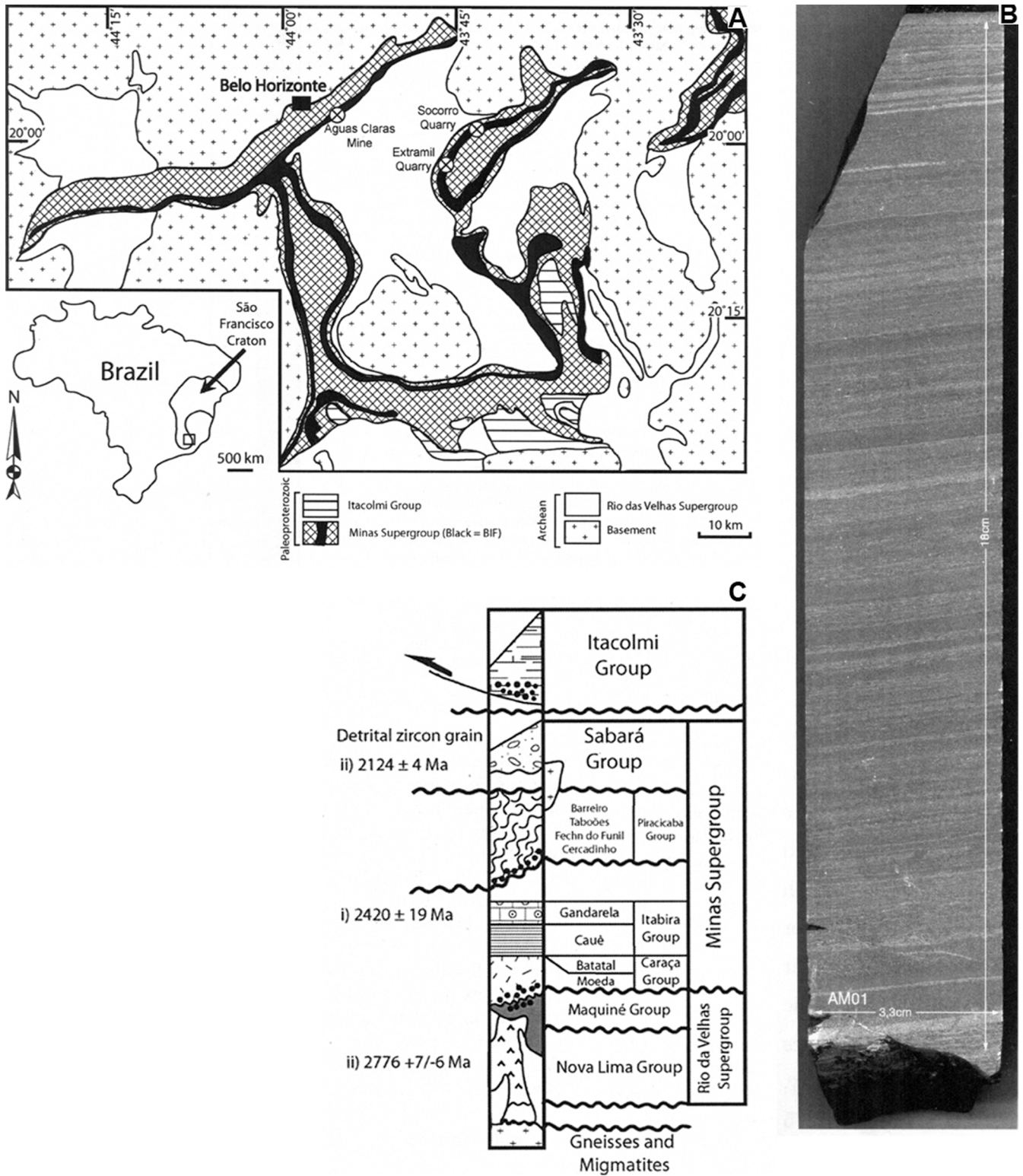


Fig. 1. (A) Geological map and location of the Aguas Claras Mine, Quadrilátero Ferrífero, Brazil (after Dorr, 1969; Spier *et al.*, 2007); (B) Drill core sample from Aguas Claras Mine (level -51 m) showing mesobands of dolomite and hematite. (C) Stratigraphic profile of the Minas Supergroup (modified after Rosière *et al.*, 2008). Age references: (i) Babinski *et al.* (1995) and (ii) Machado *et al.* (1992).

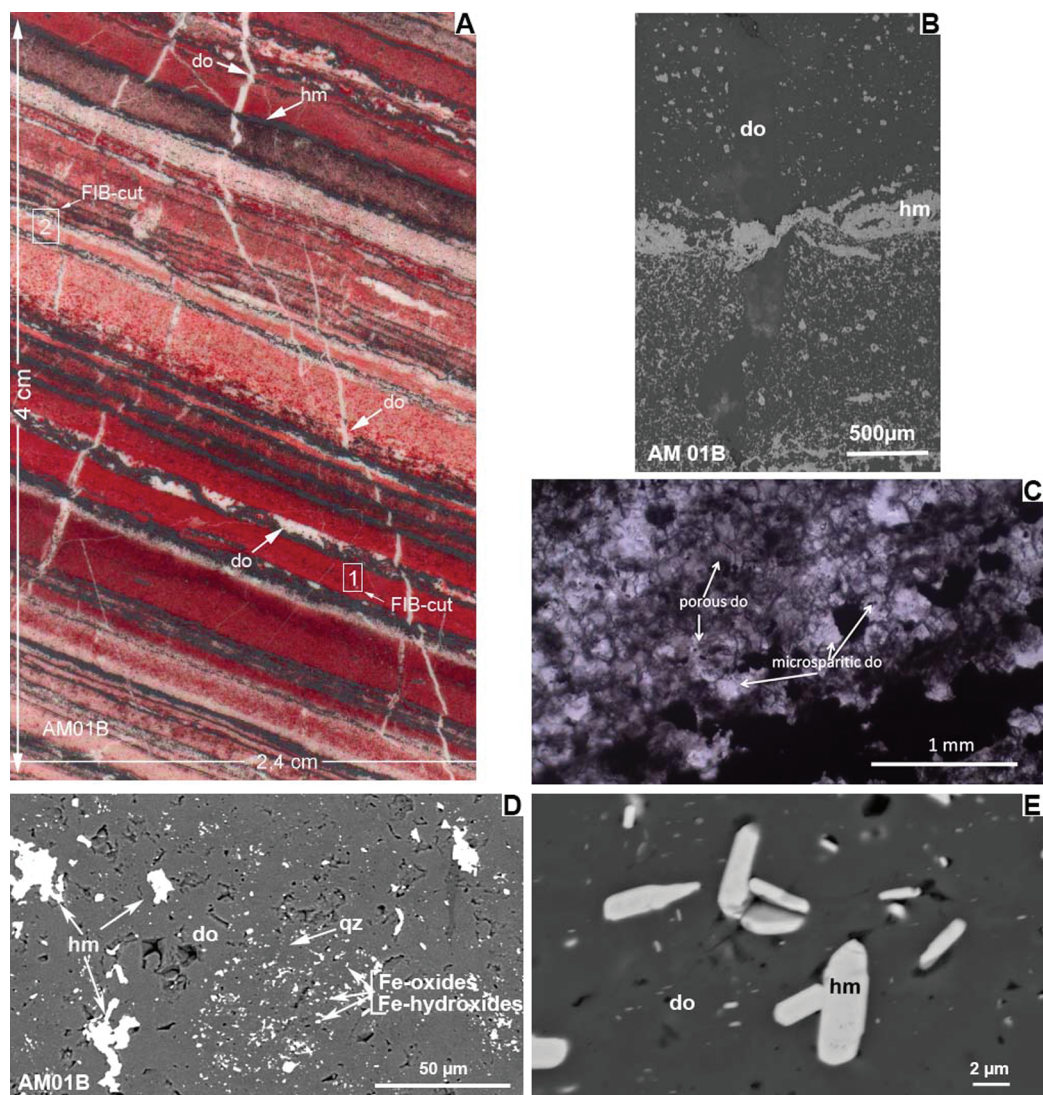


Fig. 2. Petrography of sample AM01B. (A) Thin section scan showing laminar banding of alternating dolomite (do) in red/pink in true colour and hematite (hm) in dark grey, and crosscutting and parallel veins of white dolomite. Areas 1 and 2: location of FIB foils in the dolomite. (B) SEM-BSE image, zoom of 2A showing a hematite vein parallel to lamination, which crosscuts a dolomite vein perpendicular to lamination. (C) Transmitted light photomicrograph showing porous and microsparitic dolomite in a carbonate layer. (D) SEM-BSE image of a dolomite band: (1) porous dolomite with numerous globular and lath-shaped iron oxy-hydroxides; (2) microsparitic dolomite and hematite (10–20 μm). “qz”, quartz. (E) SEM-BSE image, zoom of porous dolomite (C) showing micro- and nanometric iron (oxy)hydroxide inclusions. (Online version in colour.)

porous dolomite (area 1) and through microsparitic dolomite (area 2), both containing iron-bearing inclusions (Fig. 2A). The FIB technique is described in Wirth (2004).

The TEM study was performed with a Tecnai F20 X-Twin transmission electron microscope operating at 200 kV with a field-emission gun (FEG) as electron source. The TEM is equipped with a Gatan Imaging Filter GIF (Tridiem), a high-angle annular dark field (HAADF) detector and an EDAX analyser. The composition of the iron-bearing inclusions and the dolomite was determined in the scanning transmission mode (STEM) by energy-dispersive X-ray (EDX) analyses. The TEM mode was used to assess the bright and dark fields (BF and DF, respectively) images. Structural data of the investigated phases were derived from selected-area electron diffraction (SAED) patterns and from Fast Fourier Transforms (FFT) from high-resolution lattice-fringe images.

3.2. Curie balance and magnetic hysteresis analyses

The whole-rock sample (about 5 g) was crushed to <100 μm , homogenized and split in two fractions. Half of the sample was used untreated, whilst the second half was decarbonated prior to analysis. For decarbonation, pure 100% anhydrous orthophosphoric acid was used at 80 $^{\circ}\text{C}$ for 24 h following the method described by McCrea (1950). After decarbonation, the sample was washed with deionised water until a neutral pH was reached, and dried in an oven at 100 $^{\circ}\text{C}$ for 24 h. A reference dolomite was used for mixed-phases experiments. This dolomite was analysed beforehand by thermogravimetric analysis (TGA) and infrared spectroscopy, showing the spectrum of pure Fe-free dolomite. The thermomagnetic behaviour of the samples was determined on a horizontal force translation

Curie balance (conditions: normal air atmosphere, 0.375 T, linear temperature increase of $10^{\circ}\text{C min}^{-1}$). Magnetic hysteresis measurements were performed at room temperature with an alternating-gradient magnetometer (AGM 2900 – Micromag) in a peak-applied field of 1 T. The values of saturation magnetisation (Ms), saturation remanent magnetisation (Mrs), both mass-normalised, and coercive force (Bc) were estimated from the slope-corrected hysteresis loop. Coercivity of remanence (Bcr) was obtained by step-wise application of backfields to remove the saturation remanent magnetisation.

3.3. X-ray diffraction (XRD) analysis

The XRD measurements were performed on the two fractions of whole-rock powder, and after heating during Curie balance experiments. The XRD patterns were recorded with an X'Pert Pro PANalytical diffractometer equipped with a diffracted-beam curved graphite monochromator and an X'Celerator detector. To reduce the intensity of a fluorescence background, the X'Celerator uses pulse-height discrimination. Two different radiation sources were used: a Co- $K\alpha$ ($\lambda_{K\alpha 1} = 1.78901 \text{ \AA}$, $\lambda_{K\alpha 2} = 1.79290 \text{ \AA}$) and a Cu- $K\alpha$ ($\lambda_{K\alpha 1} = 1.5406 \text{ \AA}$, $\lambda_{K\alpha 2} = 1.5444 \text{ \AA}$) source. The analytical conditions were the following: (1) Co- $K\alpha$ source: 8 h runs, 2θ range 6° – 90° , step size 0.008° , phase identification using ICDD PDF-2 database, and (2) Cu- $K\alpha$ source: 8–30 h runs, 2θ range 4° – 80° , step size 0.008° , phase identification using COD (Crystallographic Open Database).

3.4. Raman spectroscopy

Raman spectroscopy was performed using a Horiba Jobin-Yvon Labram HR800 spectrometer. Oxide phases were characterised through unpolarised Raman spectra excited by the 514.5 nm line of an argon-ion laser and collected in a back-scattering geometry with a spectral resolution of $\sim 4 \text{ cm}^{-1}$ (diffraction grating of 600 gr/mm). The lateral resolution of the focussed laser probe was measured at $1 \mu\text{m}$ using a $100\times$ objective. The spectral signals were recorded in the range 150 – 1800 cm^{-1} . The typical acquisition time was 30–60 s. Calibration was performed during measurements in a silicon-semiconductor mode at 520.7 cm^{-1} . The Raman spectra were processed by the PeakFit 4.0 (Jandel Scientific) software using Loess smoothing procedure and a second-order polynomial function for baseline-fitting. The peak wavenumbers were determined assuming a Lorentzian line shape.

Laser-induced thermal effects are known to affect iron oxides and hydroxides (e.g. magnetite, maghemite, goethite), especially for poorly crystallised phases. Sample degradation can be avoided by using a laser power on the sample below 1 mW (De Faria *et al.*, 1997; Shebanova & Lazor, 2003; Gehring *et al.*, 2009; El Mendili *et al.*, 2010). Therefore experiments were conducted at $245 \mu\text{W}$ laser power measured at the sample

surface. Several spectra were recorded every 40 s without moving the sample for a total irradiation time of 10 min (Fig. S1 in Supplementary Material linked to this article and freely available on line on the GSW website of the journal, <http://eurjmin.geoscienceworld.org>). Single and cumulated spectra of the oxide phases do not show any difference in peak position, shape and width. Laser-induced transformation of the iron phases is thus excluded, except if the transformation is very fast.

4. Results

4.1. Electron microscopy

The interface porous/microsparitic dolomite is represented by the FIB-foil no. 1. The bright cloudy zone corresponds to the porous dolomite, while the darker grey zone corresponds to microsparitic dolomite (Fig. 3A). The HAADF overview of the dolomite shows a low-angle grain boundary between two dolomite crystals (do) with inclusions of euhedral hematite (hm) and clusters of nanometric iron hydroxides (Fig. 3A). The EDX analyses on the two dolomite types show a similar composition with the presence of small amounts of Fe and Mn, in agreement with EPMA results (Fig. 3B; Morgan *et al.*, 2013). A BF image of the large euhedral hematite ($2 \mu\text{m}$) reveals its heterogeneity, whilst the dolomite is distorted due to a high dislocation density (Fig. 3C). Clusters of iron hydroxides occurring in voids are composed of platelets and lath-shaped crystals (30 – 200 nm) (Fig. 3D and E). They decomposed under the electron beam. The FFT diffraction pattern from an HRTEM image of a single lath shows the characteristic crystallographic features of two minerals: goethite and ferrihydrite. Goethite (FeOOH) may be identified by (1 0 0), (1 4 0) and (0 4 0), whilst ferrihydrite ($\text{Fe}_2\text{O}_3 \cdot 0.5\text{H}_2\text{O}$) by (10.0), (10.2) and (00.2) (Fig. 3F). They are clearly distinguished from schwertmannite ($\text{Fe}_{16}\text{O}_{16}(\text{OH})_{12}(\text{SO}_4)_2$) and julgoldite ($\text{Ca}_2\text{Fe}(\text{Fe}, \text{Al})_2(\text{SiO}_4)(\text{Si}_2\text{O}_7)(\text{O}, \text{OH})_2 \cdot \text{H}_2\text{O}$; Jambor & Dutrizac, 1998). The EDX analyses of the lath-shaped iron hydroxide indicate traces of Si (Fig. 3G).

The FIB-foil no. 2 was cut in microsparitic dolomite (Fig. 2A, area 2). It shows one large euhedral crystal (hm, Fig. 4A and B), and a small void (Fig. 4A, area C) hosting one euhedral and one subhedral crystal (Fig. 4C, crystals 1–2 and 3, respectively). The FFT diffraction pattern of this euhedral crystal (not shown) is typical for hematite. The observed angles 33° between (11–25) and (11–21) and 48° between (11–25) and (0 0 4) agree with calculated values for hematite, 32.09° and 47.5° respectively. The crack present at the contact between dolomite and the hematite inclusion (Fig. 4B) represents post-entrapment features probably related to different thermal expansions of hematite inclusion and host dolomite. The dolomite shows straight dislocation lines (Fig. 4B). Both crystals in the void (area C in Fig. 4A and C) are hematite. The trace amounts of Ca and Mg in spectra 1–3 of Fig. 4C are related to contamination from dolomite. The subhedral hematite crystal has an onion-shell structure (Fig. 4C).

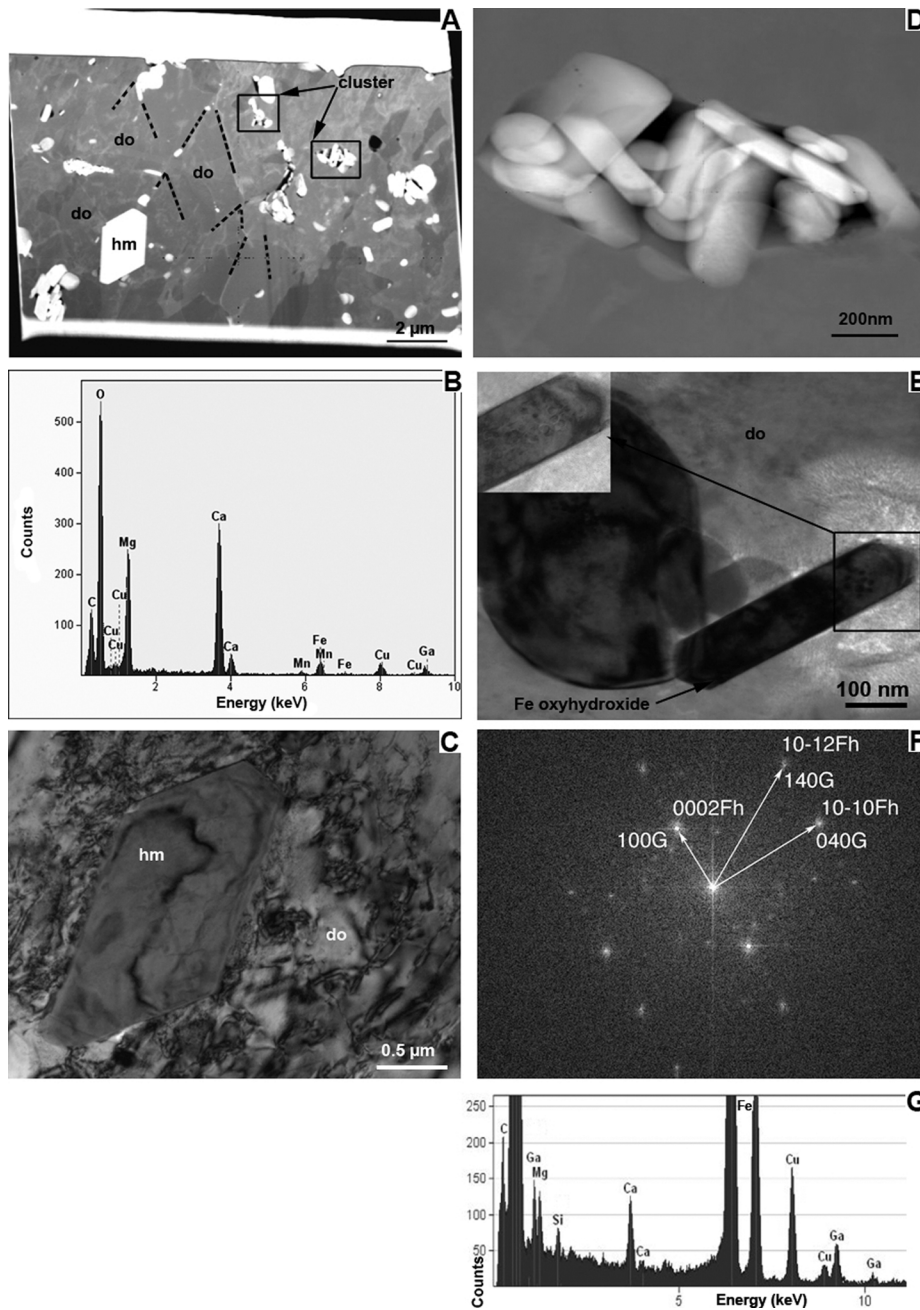


Fig. 3. FIB-foil 1 cut at the interface of the porous/microsparitic dolomite: (A) HAADF overview of the dolomite foil showing low-angle grain boundary (dashed lines) between dolomite crystals with inclusions of euhedral hematite (hm) and clusters of nanometric goethite and ferrihydrite in the porous part of the dolomite; the bright cloudy part corresponds to the porous dolomite, while the darker grey parts correspond to microsparitic dolomite; (B) EDX analysis on the HAADF image of the dolomite composition. The Cu signal is from the copper grid, whilst the Ga signal results from the FIB-TEM preparation; (C) Bright-field (BF) image showing euhedral hematite (hm) with heterogeneous contrast and high density of dislocations in dolomite (do); (D) STEM image of the cluster within the porous dolomite (A) showing iron (oxy)hydroxide platelets fully enclosed within dolomite; (E) BF image of euhedral iron (oxy)hydroxide in a cluster. Circular decomposition structures caused by the electron beam are visible in the lath (inset); (F) FFT diffraction pattern of the lath shown in (E) indicating both ferrihydrite (Fh) and goethite (G); (G) EDX analysis of the laths showing the presence of Si traces. The C, Mg and Ca peaks are from the underlying dolomite, Cu and Ga peaks as in (B).

4.2. Curie balance

The decarbonated sample was heated up to $\sim 900^\circ\text{C}$ and shows the typical thermomagnetic behaviour of hematite during heating and cooling with its Curie temperature at $\sim 680^\circ\text{C}$ (Fig. 5A, black line). Similarly, the untreated

whole-rock sample heated up to $\sim 750^\circ\text{C}$ exhibited typical thermomagnetic behaviour for hematite upon heating and cooling. However, upon cooling an additional increase of the magnetisation is observed below $\sim 350^\circ\text{C}$ (Fig. 5A, blue line). This behaviour is due to a new magnetic mineral, which appears during the experiment. The new

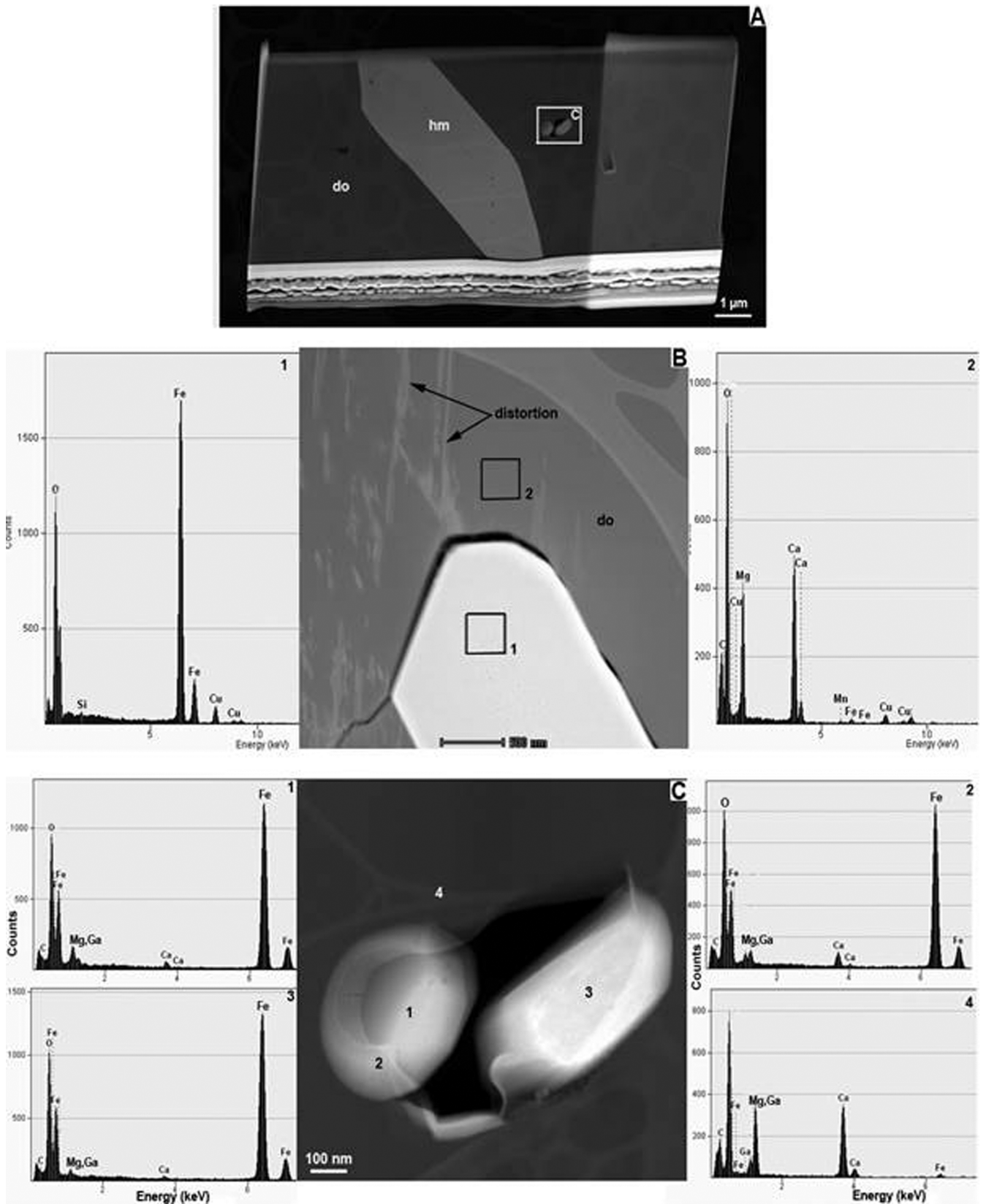


Fig. 4. FIB-foil 2 cut in the microspartic dolomite (do): (A) TEM image showing one euhedral hematite (hm) crystal and a void hosting euhedral and a subhedral crystal; (B) detail of the contact between the euhedral hematite crystal (EDX spectrum 1) and the host dolomite (EDX spectrum 2). The dolomite shows straight lines of dislocations and a crystal growth crack; (C) zoom of area C in (A) showing that the two crystals are hematite (spectra 1–3). Note that the dolomite is almost iron-free (spectrum 4).

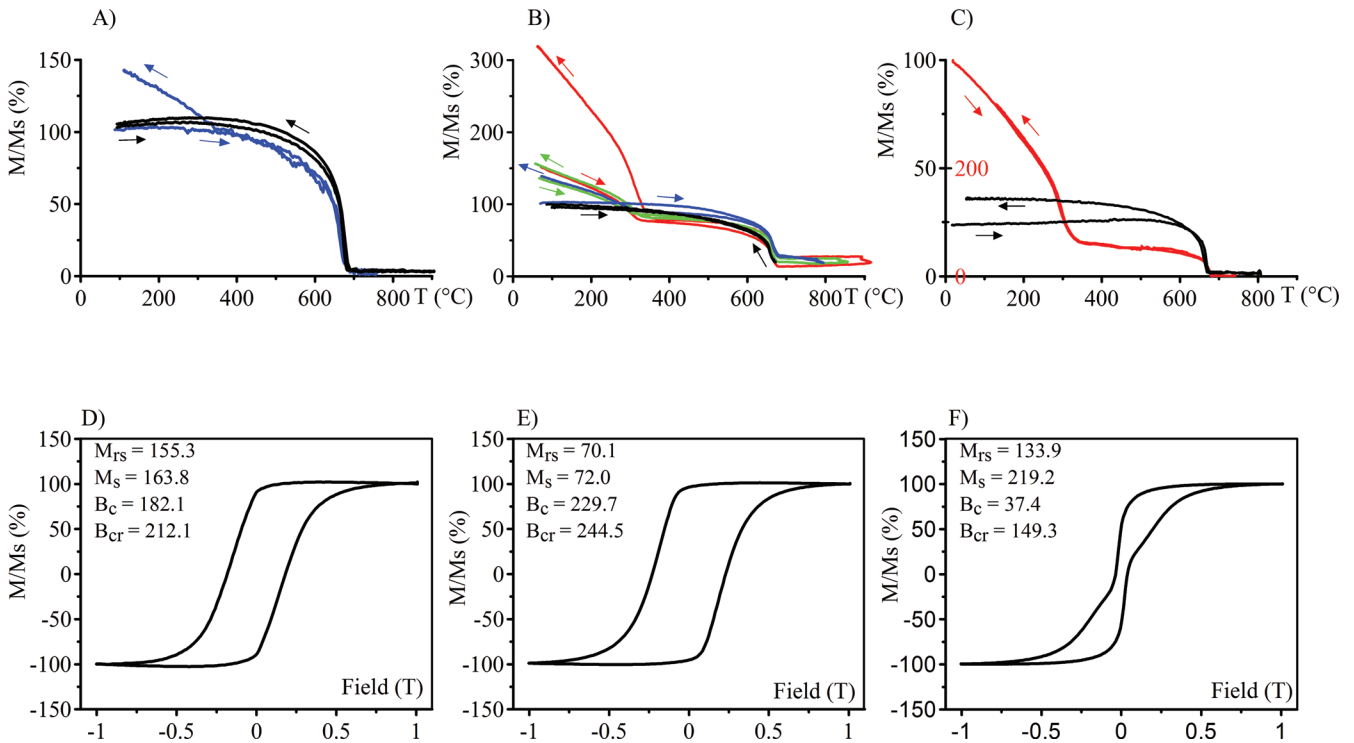


Fig. 5. Curie balance analyses of: (A) a whole-rock sample heated up to $\sim 750^\circ\text{C}$ (blue line) and a decarbonated sample heated up to $\sim 900^\circ\text{C}$ (black line), both hold at these temperatures for 30 min before cooling; (B) whole-rock sample heated up to $\sim 680^\circ\text{C}$ (black line), cooled and successively heated and being held for 30 min at temperatures of $\sim 800^\circ\text{C}$, $\sim 850^\circ\text{C}$ and $\sim 900^\circ\text{C}$ before cooling (blue, green and red lines, respectively); (C) decarbonated sample mixed with reference dolomite and heated up to $\sim 800^\circ\text{C}$ (black line) and up to $\sim 900^\circ\text{C}$, held at $\sim 900^\circ\text{C}$ for 30 min, cooled and re-heated at $\sim 900^\circ\text{C}$ (red line); magnetic hysteresis loop of (D) decarbonated and (E) whole-rock samples both before heating; (F) whole-rock sample heated above $\sim 900^\circ\text{C}$. Saturation magnetisation (M_s) and remanent saturation magnetization (M_{rs}) expressed in $\text{nA m}^2 \text{mg}^{-1}$, remanent coercivity (B_{cr}) and coercivity (B_c) expressed in mT. (Online version in colour.)

magnetic mineral is thus related to the dolomitic part of the whole-rock sample, or was destroyed during the decarbonation process. To determine the temperature interval and conditions in which the new magnetic mineral is formed, several Curie balance analyses were performed on (1) the whole-rock sample and (2) a decarbonated sample mixed with the reference dolomite of the GEOPS laboratory. In experiment (1), the whole-rock sample was heated to $\sim 680^\circ\text{C}$ (Fig. 5B, black line), cooled and successively re-heated to $\sim 800^\circ\text{C}$, $\sim 850^\circ\text{C}$ and $\sim 900^\circ\text{C}$, and kept constant for ~ 30 min upon reaching the defined temperature before cooling (Fig. 5B, blue, green and red lines respectively). The whole-rock sample heated to $\sim 680^\circ\text{C}$ shows the thermomagnetic behaviour for hematite (Fig. 5B, black line). However, after heating to temperatures above 680°C , a new magnetic mineral was observed during cooling below $\sim 350^\circ\text{C}$. This finding indicates that the new magnetic mineral appears at temperature above 680°C . This agrees with the previous result for whole-rock experiment heated up to $\sim 750^\circ\text{C}$ (Fig. 5A). Upon each incremental temperature increase, the proportion of the magnetic mineral increases (Fig. 5B), and is much higher for the last step at $\sim 900^\circ\text{C}$ (Fig. 5B, red line). In experiment (2) the decarbonated sample mixed with the reference dolomite powder was heated up to $\sim 800^\circ\text{C}$ and $\sim 900^\circ\text{C}$, and maintained at these temperatures for 30 min before cooling. On heating up to

$\sim 800^\circ\text{C}$, only hematite is observed (Fig. 5C, black line). However, when heated until $\sim 900^\circ\text{C}$, the sample shows an increase in the magnetisation during cooling below $\sim 350^\circ\text{C}$, exactly as in the whole-rock sample heated up to $\sim 900^\circ\text{C}$ shown in Fig. 5B (cooling part of the red line). The new magnetic mineral from both experiments demagnetises above $\sim 350^\circ\text{C}$ when heated again, and becomes re-magnetised at the same temperature upon cooling (Fig. 5C, red line). The new magnetic mineral remains stable and has a far greater magnetisation than hematite.

4.3. Magnetic hysteresis

Magnetic hysteresis before heating of the untreated and the decarbonated whole-rock samples show the same behaviour (Fig. 5E and F). This behaviour can be attributed to the single-domain hematite (Peters & Dekkers, 2003) and is consistent with the identification of hematite by Curie balance analyses on whole-rock sample heated until $\sim 680^\circ\text{C}$ and on decarbonated samples.

The whole-rock sample, when heated to $\sim 900^\circ\text{C}$, shows a wasp-waisted hysteresis loop, which is constricted in the middle section, and wider above and below the middle section (Fig. 5F). Wasp-waisted hysteresis loops indicate the coexistence of at least two different magnetic components with contrasting coercive fields (*e.g.*

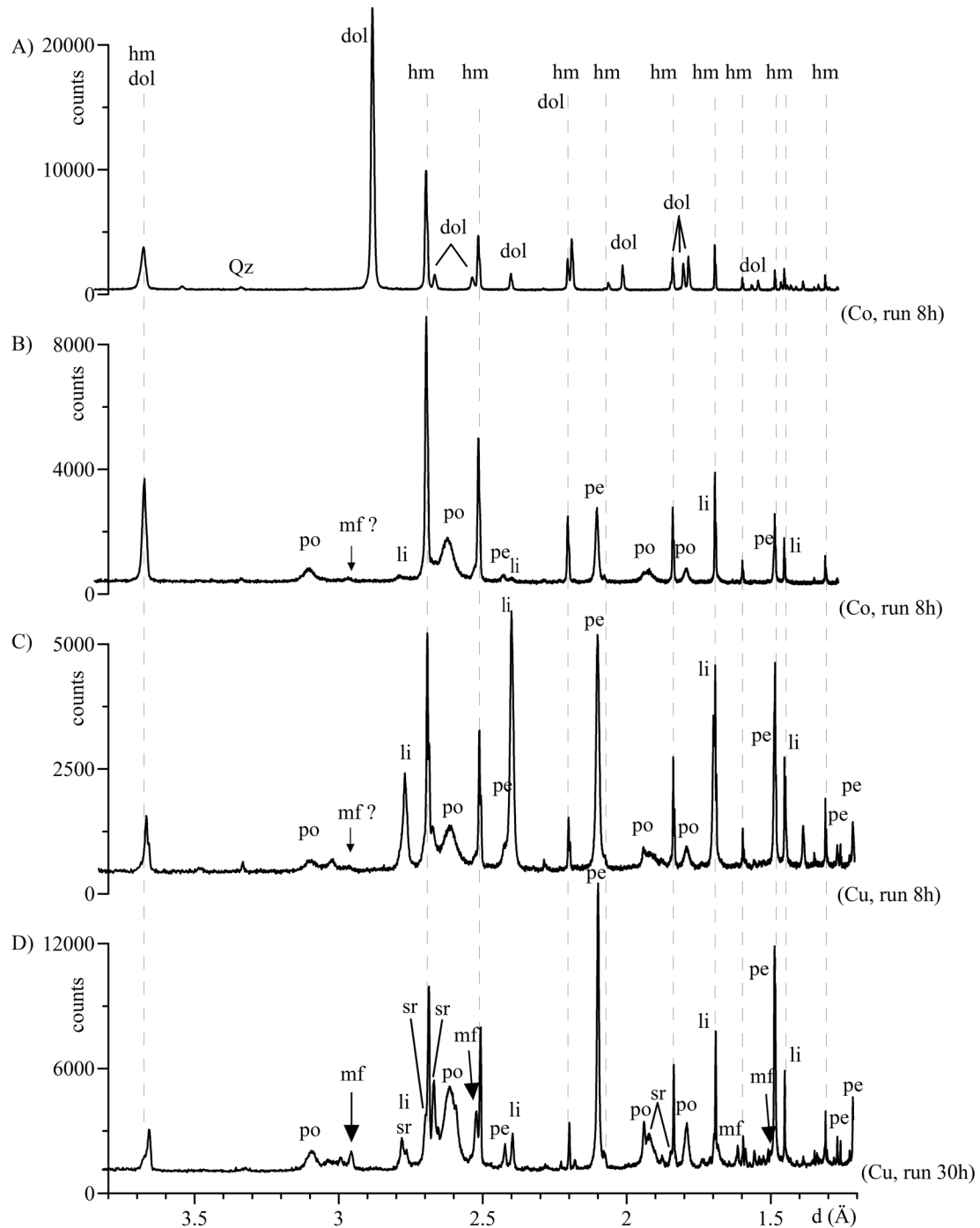


Fig. 6. X-ray diffraction spectra of the: (A) whole-rock sample, the same as analysed by FIB-TEM, SEM and Raman spectroscopy, measured with Co anode; (B–D) residue produced from the Curie balance analysis held at $\sim 900^\circ\text{C}$ for 30 min and measured with Co anode (B) and Cu anode (C), and for 3 h, measured with Cu anode (D). Co – cobalt, Cu – copper, hm – hematite, dol – dolomite, li – lime, pe – periclase, po – portlandite, mf – magnesioferrite, sr – srebrodolskite. The high intensities of the peaks at 1.69 Å and 1.49 Å are related to the overlap of hematite and lime, and hematite and periclase, respectively.

Wasilewski, 1973; Day *et al.*, 1977; Roberts *et al.*, 1995; Tauxe *et al.*, 1996). In such conditions, the coercivity of remanence (B_{cr}) is controlled by the “hard”, high-coercivity component, such as hematite or goethite, whilst the coercive force (B_c) is controlled by the “soft”, low-coercivity ferrimagnetic component (*e.g.* magnetite or

maghemite). The degree of the constriction in the middle section of the hysteresis loop reflects the relative contribution of “hard” and “soft” components. The presence of two different components (hematite and a new magnetic mineral) was also observed through Curie balance experiments on whole-rock sample heated above $\sim 680^\circ\text{C}$.

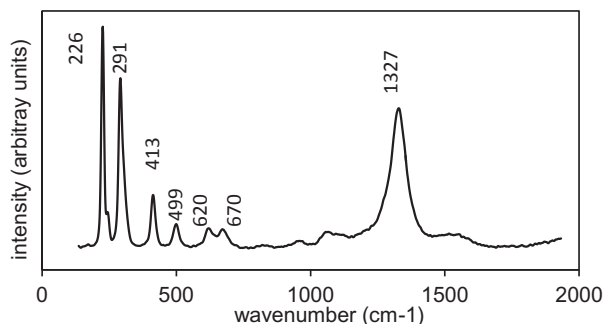


Fig. 7. Raman spectra of hematite from an inclusion in the porous dolomite.

4.4. X-ray diffraction analysis

The XRD experiments were performed with Co and Cu tubes on the same sample as investigated by SEM, FIB-TEM and Raman spectroscopy. In both configurations, XRD measurements on powdered whole-rock samples show dolomite and hematite (Fig. 6A for XRD with Co anode). The XRD analyses (8 h runs, Co and Cu anodes) on whole-rock sample heated during Curie balance experiments and held at $\sim 900^\circ\text{C}$ for 30 min (Fig. 6B and C), show hematite as in Fig. 6A, plus lime (CaO), periclase (MgO) and portlandite, $\text{Ca}(\text{OH})_2$. However, the XRD analyses with Cu anode and run for 30 h on a whole-rock sample held at $\sim 900^\circ\text{C}$ for ~ 3 h show magnesioferrite (MgFe_2O_4) and srebrodolskite ($\text{Ca}_2\text{Fe}_2\text{O}_5$) (Fig. 6D). The improvement of the signal-to-noise ratio of this analysis is due to the longer heating period and counting time.

4.5. Raman spectroscopy

Raman spectra were collected on iron minerals from the microsparitic dolomite and from the micrometric iron-rich inclusions in porous dolomite, and in quartz. Typical spectra show bands at 224–226, ~ 300 , 411–414, 498–502, 611–621, 668–673, and 1321–1329 cm^{-1} (Fig. 7). The band at $\sim 300 \text{ cm}^{-1}$ is decomposed in two bands at 290–293 and 299–306 cm^{-1} ; the latter usually appears on the flank of the stronger $\sim 290 \text{ cm}^{-1}$ band. In some spectra, an additional band at 244–247 cm^{-1} appears. This combination of bands is typical of hematite (e.g. De Faria *et al.*, 1997; Hanes, 2009). Hematite belongs to the D_{3d}^6 spatial group and seven Raman active modes are expected: two A_{1g} modes at 225 and 498 cm^{-1} and five E_g modes at 247, 293, 299, 412 and 613 cm^{-1} , while the interpretation of the band at $\sim 1320 \text{ cm}^{-1}$ is controversial but usually interpreted as resulting from a two-magnon scattering (De Faria *et al.*, 1997). With this technique, hematite was the only iron mineral detected among these inclusions.

5. Discussion

Commonly, optical microscopy, SEM, XRD and Mössbauer spectroscopy are used to characterise BIF (e.g. Morris, 1980; Beukes & Gutzmer, 2008; Rosière *et al.*, 2008; Angerer *et al.*, 2012; Morgan *et al.*, 2013).

Combining these techniques with Raman spectroscopy, FIB-TEM and Curie balance analyses allow us to demonstrate for the first time, to our knowledge, the presence of eu/subhedral iron oxide and iron hydroxide as clusters in voids included within dolomite crystals.

5.1. Evidence of iron oxide and iron hydroxides in dolomite

Direct mineralogical analyses (XRD, Raman spectroscopy and FIB-TEM analyses) revealed hematite, while goethite/ferrihydrate was only detected by FIB-TEM analyses in the inclusions from the porous dolomite (Fig. 3). In the microsparitic dolomite, only hematite was observed with the above-mentioned methods (Fig. 4). Curie balance analyses indirectly indicated the presence of iron hydroxides through phase transformation at temperatures above $\sim 680^\circ\text{C}$ and below $\sim 900^\circ\text{C}$. Indeed, Curie balance experiments on the whole-rock sample heated above $\sim 680^\circ\text{C}$ identified, besides hematite, a new magnetic mineral (magnesioferrite or Mg-rich maghemite, see Section 5.2) at $\sim 350^\circ\text{C}$ during cooling (Fig. 5A). The amount of this new magnetic phase increased during step-heating until $\sim 900^\circ\text{C}$ (Fig. 5B). On the contrary, experiments on the decarbonated sample mixed with reference dolomite did not show the new magnetic mineral, unless heated at temperatures above $\sim 900^\circ\text{C}$ (Fig. 5C). This finding shows that two different processes are involved in the formation of the new magnetic mineral, but only the one occurring at temperatures above $\sim 680^\circ\text{C}$ and below $\sim 900^\circ\text{C}$ is related to the presence of the iron hydroxides included in the porous dolomite.

5.2. Formation of the new magnetic mineral related to dolomite decomposition

Differential thermal analysis (DTA) on dolomite commonly shows two peaks during decomposition (McIntosh *et al.*, 1990). The first peak between 687°C to 781°C (culminating at 773°C) corresponds to the transformation of dolomite to calcite (CaCO_3) and periclase (MgO), whilst the second peak between 781°C and 916°C (culminating at 834°C) is related to the decomposition of calcite to lime (CaO) (Samtani *et al.*, 2002; Gunasekaran & Anbalagan, 2007). In our study, periclase and lime observed in the XRD spectra performed on residues after Curie balance heating experiments at $\sim 900^\circ\text{C}$ (Fig. 6) are, thus, related to the thermal decomposition of the dolomite.

In the whole-rock experiments the new magnetic mineral appears on heating above $\sim 680^\circ\text{C}$, *i.e.* a temperature at which the dolomite decomposition starts and liberates the goethite/ferrihydrate inclusions (see FIB-TEM results). It can be excluded that FeCO_3 is present in the samples. During Curie-balance experiment, siderite would have been decomposed before 680°C , prior to Mg and Ca carbonates, and magnetite would have formed on the cooling path, and have been detected as an increase of magnetisation from 580°C (Tudryn & Tucholka, 2004).

Moreover, the new magnetic mineral is not observed in the whole-rock experiments performed at temperature below $\sim 680^\circ\text{C}$. At this temperature dolomite is still stable and goethite/ferrihydrate remains enclosed within the dolomite. Experiments on decarbonated samples mixed with the reference dolomite show that hematite remains stable during heating at temperatures below $\sim 900^\circ\text{C}$, and is partly transformed into the new magnetic mineral at higher temperatures.

We can therefore assume that the new magnetic mineral results from goethite/ferrihydrate transformation due to the reducing environment generated by dolomite decomposition and CO_2 production above $\sim 680^\circ\text{C}$ and below $\sim 900^\circ\text{C}$ during heating. As shown by its thermomagnetic behaviour and the wasp-waisted magnetic hysteresis loops and magnetic hysteresis parameters of the samples heated above $\sim 680^\circ\text{C}$ (Fig. 5F), the new mineral can be magnesioferrite or Mg-rich maghemite, both minerals having a spinel structure and a Curie temperature of $\sim 350^\circ\text{C}$ (Fabris *et al.*, 1995; Antao *et al.*, 2005). However, maghemite is metastable and was not detected by XRD analyses, whereas magnesioferrite (mf) was identified (Fig. 6D).

5.3. Origin and evolution of the hematite and iron hydroxide inclusions in dolomite

For the first time, hematite and goethite/ferrihydrate inclusions are reported in dolomite from a low-grade BIF from the Itabira Group. Usually in Neoproterozoic reducing environment, iron should be in the ferrous state and incorporated in carbonates (siderite or ankerite) or in magnetite. However, these minerals were not observed in our samples (Morgan *et al.*, 2013), which raises the question regarding the origin of the ferric iron-bearing inclusions. Furthermore the survival of these inclusions in samples that experienced greenschist-facies metamorphism has to be explained.

Based on our FIB-TEM studies, clusters of euhedral nano-sized hematite (in microsparitic dolomite; Fig. 4B and C) and of goethite/ferrihydrate (in porous dolomite; Fig. 3) occur in voids. We interpret this finding as the presence of former ferric-iron rich fluid inclusions, which were trapped by the dolomite probably on crystal lattice defects (Tucker & Wright, 1999). The iron oxy-hydroxide clusters formed after the dolomite precipitation through fluid-inclusion cracking or as daughter mineral in the inclusion.

The exact nature of the iron-hydroxide inclusions could not be unequivocally identified. The FFT diffraction pattern of the lath-shaped mineral can be indexed as coexisting goethite and ferrihydrate (Fig. 3F). However, the lath morphology of the analysed particles supports the presence of goethite. The “mixed” or “superposed” FFT diffraction pattern would indicate an incipient solid-state transformation rather than a dissolution-precipitation process (Cornell & Schwertmann (2003). This solid-state transformation of ferrihydrate to goethite could be a

thermal dehydration/dehydroxylation process, similarly to the well-known transformation of ferrihydrate to hematite (Cornell & Schwertmann, 2003).

Hematite and iron hydroxides can form from Fe^{2+} -bearing solutions by oxidation in modern hydrothermal vent environments, or distal to vents in platform environments. The nature of the iron hydroxides depends on the pH, temperature and composition of the fluids. The precipitation of goethite is known to occur in carbonate environments as a fast oxidation at pH around 4 (Cornell & Schwertmann, 2003; Kennedy *et al.*, 2004).

Although oxygenated ocean waters in the Neoproterozoic are considered unlikely, recent studies by Hashizume *et al.* (2016) on a Neoproterozoic BIF (2.7–2.9 Ga, Dharwar Craton, India), proposed temporarily free O_2 production in Neoproterozoic ocean waters due to biological activity. Early diagenetic iron oxide formation related to biological O_2 production was also suggested by Lyons *et al.* (2014).

Iron (oxy)hydroxides may have been preserved as they contain silica (Fig. 3), known to strongly reduce their dissolution (*e.g.* Eick *et al.*, 1999; Schwertmann & Thalmann, 1976).

Straight dislocation lines are pinned by the hematite inclusions in microsparitic dolomite (Figs. 3C and 4B). Such dislocation lines are known to form below the critical temperature of 420°C (*e.g.* Barber & Wenk, 2001). The dislocation lines are probably related to deformation events either at around 2.1 Ga, Transamazonian/Mineiro orogeny, or at around 0.6 Ga, the Brasiliano/Pan African Orogeny (Chemale *et al.*, 1994).

6. Concluding summary

- A cross-method approach is indispensable for a comprehensive characterisation of micro- and nano-metric inclusions.
- Curie balance analyses allow the indirect detection of the presence of iron (oxy)hydroxides, such as goethite and ferrihydrate, in addition to hematite in dolomite BIF: magnesioferrite, commonly forming at temperatures above $\sim 900^\circ\text{C}$, formed at lower temperatures (between 680°C and 900°C) in our study.
- The hematite and goethite/ferrihydrate clustered inclusions possibly precipitated from Fe-rich and Si-bearing fluid inclusions, after the formation of dolomite, and required an oxygenated environment around 2.4 Ga. This raises the question of the origin of (local?) O_2 production in Neoproterozoic ocean waters.
- FFT diffraction pattern showing both goethite and ferrihydrate may indicate a solid-state transformation from ferrihydrate to goethite in the inclusions.
- The silica contents in goethite/ferrihydrate may have allowed for iron hydroxide preservation during the subsequent history, for which microstructural evidence (dislocation climb in dolomite) suggests deformation below 420°C .
- This finding may have implications for the valorisation and metallurgical processing of low-grade iron ores, which are at present by-passed or stockpiled as tailings,

as about 30% of the iron is locked-up in dolomite micro- and nano-inclusions. The presence of iron (oxy)hydroxide inclusions should allow lower sintering temperatures.

Acknowledgements: The authors gratefully acknowledge Vale for providing their permission to study the samples as well as logistical and practical support and information relating to these samples. SEM was performed at GEOPS laboratory, Université Paris-Sud, and ITeP, Université Paris 06, France; FIB-TEM at the GFZ, Potsdam, Germany; Curie balance at the GEOPS laboratory, Université Paris-Sud, France; Magnetic hysteresis at the LSCE-CNRS/CEA laboratory at Gif-sur-Yvette, France; XRD at the IMPMC laboratory, Université Paris 06 and the GEOPS laboratory, Université Paris-Sud, France; Raman spectroscopy at the Laboratoire de Sciences de la Terre, ENS-Lyon, France. Thanks for technical support go to Anja Schreiber at the GFZ, for the FIB-TEM preparation, Gilles Montagnac (ENS-Lyon) for the Raman analyses and Laurent Daumas for image preparation. UFMG and Carlos Rosière are thanked for the research stay of Rachael Morgan. We thank the Laboratoire de Géologie de Lyon (ENS-Lyon) for access to the national Raman instrument supported by the Institut National des Sciences de l'Univers (INSU), CNRS. This study was possible through a PhD President's scholarship from the Université Paris-Sud to Rachael Morgan. It was funded by the national and international projects PNP, COFECUB-CAPEs, the Brazilian CNPq 5503482010-7 and the European Science Foundation (Archean Habitats for Life). We thank the reviewers and the handling editor, Elisabetta Rampone, for constructive comments and suggestions.

References

- Alkim, F.F. & Marshak, S. (1998): Transamazonian Orogeny in the Southern Sao Francisco Craton Region, Minas Gerais, Brazil: evidence for Paleoproterozoic collision and collapse in the Quadrilátero Ferrífero. *Precambrian Res.*, **90**, 29–58.
- Angerer, T., Hagemann, S.G., Danyushevsky, V. (2012): Geochemical evolution of the Banded iron formation-hosted high-grade iron ore system in the Koolyanobbing Greenstone Belt, Western Australia. *Econ. Geol.*, **107**, 599–644.
- Antao, S.M., Hassan, I., Parise, J.B. (2005): Cation ordering in magnesioferrite, $MgFe_2O_4$, to 982 °C using in situ synchrotron X-ray powder diffraction. *Am. Mineral.*, **90**, 219–228.
- Babinski, M., Chemale, Jr., F., Van Schmus, W.R. (1991): Geocronologia Pb/Pb em rochas carbonáticas do Supergrupo Minas, Quadrilátero, Minas Gerais, Brasil. in "Anais III Congresso Brasileira de Geoquímica, Sao Paulo, Soc. Bras. De Geoquímica Resumos", 2, 628–631.
- , —, — (1993): A idade das formacoes ferríferas bandadas do Supergrupo Minas e sua correlacao com aquelas da Africa do Sul et Australia. in "Anais II Simposio do Craton do Sao Francisco, Salvador, Soc. Bras. Geol., Nucleo Bahia/Sergipe", 152–153.
- , —, — (1995): The Pb/Pb age of the Minas Supergroup carbonate rocks, Quadrilátero Ferrífero, Brazil. *Precambrian Res.*, **72**, 235–245.
- Barber, D.J. & Wenk, H.-R. (2001): Slip and dislocation behaviour in dolomite. *Eur. J. Mineral.*, **13**, 221–243.
- Beukes, N. & Gutzmer, J. (2008): Origin and paleoenvironmental significance of major iron formations at the Archean-Paleoproterozoic boundary. *Rev. Econ. Geol.*, 15–47.
- Bolhar, R., Kamber, B.S., Moorbath, S., Fedo, C.M., Whitehouse, M.J. (2004): Characterisation of early Archean chemical sediments by trace element signatures. *Earth Planet. Sci. Lett.*, **22**, 43–60.
- Chemale, Jr., F., Rosière, C.A., Endo, I. (1994): The tectonic evolution of the Quadrilátero Ferrífero, Minas Gerais, Brazil. *Precambrian Res.*, **6**, 25–54.
- Cornell, R. & Schwertmann, U. (2003): The iron oxides: structure, properties, reactions, occurrences and use. VCH, ed., Weinheim, 600 p.
- Dalstra, H. & Guedes, S.T. (2004): Giant hydrothermal hematite deposits with Mg-Fe metasomatism: a comparison of the Carajas, Hamersley, and other iron ores. *Econ. Geol.*, **99**, 1793–1800.
- Day, R., Fuller, M.D., Schmidt, V.A. (1977): Magnetic hysteresis properties of synthetic titanomagnetites. *Phys. Earth Planet. Inter.*, **13**, 260–266.
- De Faria, D.L.A., Venancio-Silva, S., de Oliveira, M.T. (1997): Raman microspectroscopy of some iron oxides and oxyhydroxides. *J. Raman Spectrosc.*, **28**, 873–878.
- Dorr, J.V.N. (1969): Physiographic, stratigraphic and structural development of the Quadrilátero Ferrífero, Minas Gerais. U.S. Geol. Survey Prof. Paper 641-A.
- Eick, M.J., Peak, J.D., Brady, W. (1999): The effect of oxyanions on the oxalate-promoted dissolution of goethite. *Soil Sci. Soc. Am. J.*, **63**, 1133–1141.
- El Mendili, Y., Bardeau, J.F., Riandrianantoandro, N., Gourbil, A., Grenèche, J.M., Mercier, A.M., Grasset, F. (2010): New evidence of in situ laser irradiation effects on $\gamma\text{-Fe}_2\text{O}_3$ nanoparticles: a Raman spectroscopic study. *J. Raman Spectrosc.*, **42**, 239–242.
- Fabris, J., Coey, J., Qi, Q., Mussel, W. (1995): Characterization of Mg-rich maghemite from tuffite. *Am. Mineral.*, **80**, 664–669.
- Gehring, A.U., Fisher, H., Louvel, M., Kunze, K., Weidler, P.G. (2009): High temperature stability of natural maghemite: a magnetite and spectroscopic study. *Geophys. J. Int.*, **179**, 1361–1371.
- Gloter, A., Zbinden, M., Guyot, F., Gaill, F., Colliex, C. (2004): TEM-EELS study of natural ferrihydrite from geological-biological interactions in hydrothermal systems. *Earth Planet. Sci. Lett.*, **222**, 947–957.
- Gunasekaran, S. & Anbalagan, G. (2007): Thermal decomposition of natural dolomite. *Bull. Mater. Sci.*, **30**, 339–344.
- Hanesh, M. (2009): Raman spectroscopy of iron oxides and (oxy) hydroxides at low laser power and possible implications in environmental magnetic studies. *Geophys. J. Int.*, **177**, 942–948.
- Hashizume, K., Pinti, D.L., Orberger, B., Cloquet, C., Jayananda, M., Soyama, H. (2016): A biological switch at the ocean surface as a cause of laminations in a Precambrian iron formation. *Earth Planet. Sci. Lett.*, **446**, 27–36.
- Isley, A.E. (1995): Hydrothermal plumes and the delivery of iron to banded iron formation. *J. Geol.*, **103**, 169–185.
- Jambor, J.L. & Dutrizac, J.E. (1998): Occurrence and constitution of natural and synthetic ferrihydrite, a widespread iron oxyhydroxide. *Chem. Rev.*, **98**, 2549–2585.
- Kennedy, C.B., Scott, S.D., Ferris, F.G. (2004): Hydrothermal phase stabilization of 2-line ferrihydrite by bacteria. *Chem. Geol.*, **212**, 269–277.

- Klein, C. (2005): Some Precambrian banded iron-formations (BIFs) from around the world: their age, geologic setting, mineralogy, metamorphism, geochemistry, and origins. *Am. Mineral.*, **90**, 1473–1499.
- Lyons, T.W., Reinhard, C.T., Planavsky, J. (2014): The rise of oxygen in Earth's early ocean and atmosphere. *Nature*, **506**, 307–315.
- Machado, N., Noce, C.M., Ladeira, E.A., Belo de Oliveira, O.A. (1992): U–Pb geochronology of Archean magmatism and Proterozoic metamorphism in the Quadrilátero Ferrífero, southern Sao Francisco craton. *Geol. Soc. Am. Bull.*, **104**, 1221–1227.
- Manceau, A. & Drits, V.A. (1993): Local structure of ferrihydrite and ferroxhite by EXAFS spectroscopy. *Clay Miner.*, **28**, 165–184.
- McCrea, J.M. (1950): On the isotope chemistry of carbonates and a paleo-temperature scale. *J. Chem. Phys.*, **18**, 849–857.
- Morgan, R.R., Orberger, B., Rosière, C.A., Wirth, R., da Mota Carvalho, C., Bellver-Baca, M.T. (2013): The origin of coexisting carbonates in banded iron formations: a micro-mineralogical study of the 2.4 Ga Itabira Group, Brazil. *Precambrian Res.*, **224**, 491–511.
- McIntosh, R.M., Sharp, J.H., Wilburn, F.W. (1990): The thermal decomposition of dolomite. *Thermochim. Acta*, **165**, 81–296.
- Morris, R.C. (1980): A textural and mineralogical study of the relationship of iron ore to banded iron ore formation in the Hamersley iron province of Western Australia. *Econ. Geol.*, **75**, 184–209.
- Morris, R.C. (1985): Genesis of iron ore in banded iron formation by supergene and supergene-metamorphic processes, a conceptual model. in “Handbook of Strata-Bound and Stratiform Ore Deposits”, vol. 13, K.H. Wolf, ed. Elsevier, Amsterdam, 73–235.
- Morris, R.C. (1998): BIF-hosted iron ore deposits-Hamersley style. *AGSO J. Aust. Geol. Geophys.*, **17**, 207–211.
- Orberger, B., Wagner, C., Wirth, R., Quirico, E., Gallien, J.P., Derré, C., Montagnac, G., Noret, A. (2012): Origin of iron-oxide spherules in the banded iron formation of the Bababudan Group, Dharwar Craton, Southern India. *J. Asian Earth Sci.*, **52**, 31–42.
- Orberger, B., Wagner, C., Tudryn, A., Wirth, R., Morgan, R., Fabris, J.D., Grenèche, J.M., Rosière, C.A. (2014): Micro- to nano-scale characterization of martite from a banded iron formation in India and a lateritic soil in Brazil. *Phys. Chem. Minerals*, **41**, 651–667.
- Peters, C. & Dekkers, M.J. (2003): Selected room temperature magnetic parameters as a function of mineralogy, concentration and grain size. *Phys. Chem. Earth*, **28**, 659–667.
- Pimenta da Silva, F., Lopes-Silva, L., Rosière, C.A. (2011): Stratigraphic analysis of a carbonate sequence related to the BIFs of the Iron Quadrangle, Southwestern Brazil. in “Proceedings SGA, Antofagasta, A-190”.
- Roberts, A.P., Cui, Y., Verosub, K.L. (1995): Wasp-waisted hysteresis loops: mineral magnetic characteristics and discrimination of components in mixed magnetic systems. *J. Geophys. Res.*, **100**, 17909–17924.
- Rosière, C.A., Spier, C.A., Rios, F.J., Suckau, V.E. (2008): The Itabirites of the Quadrilátero Ferrífero and related high-grade iron ore deposits: an overview. *SEG Rev.*, **15**, 223–254.
- Samtani, M., Dollimore, D., Alexander, K.S. (2002): Comparison of dolomite decomposition kinetics with related carbonates and the effect of procedural variables on its kinetic parameters. *Thermochim. Acta*, **392–393**, 135–145.
- Schwertmann, U. & Thalmann, H. (1976): The influence of [Fe(II)], [Si], and pH on the formation of lepidocrocite and ferrihydrite during oxidation of aqueous FeCl₂ solutions. *Clay Miner.*, **11**, 189–200.
- Shebanova, O.N. & Lazor, P. (2003): Raman study of magnetite (Fe₃O₄): laser-induced thermal effects and oxidation. *J. Raman Spectrosc.*, **34**, 845–852.
- Spier, C.A., de Oliveira, S.M.B., Sial, A.N., Rios, F.J. (2007): Geochemistry and genesis of the banded iron formations of the Caúe Formation, Quadrilátero Ferrífero, Minas Gerais, Brazil. *Precambrian Res.*, **152**, 170–206.
- Spier, C.A., de Oliveira, S.M.B., Rosière, C.A., Ardisson, J.D. (2008): Mineralogy and trace-element geochemistry of the high-grade iron ores of the Águas Claras Mine and comparison with the Capão Xavier and Tamanduá iron ore deposits, Quadrilátero Ferrífero, Brazil. *Mineral. Depos.*, **43**, 229–254.
- Taitel-Goldman, N. & Singer, A. (2002): Metastable Si–Fe phases in hydrothermal sediments of Atlantis II Deep, Red Sea. *Clay Miner.*, **37**, 235–248.
- Tauxe, L., Mullender, T.A.T., Pick, T. (1996): Potbellies, wasp-waisted, and superparamagnetism in magnetic hysteresis. *J. Geophys. Res.*, **101**, 571–583.
- Teixeira, W. & Figueiredo, M.C.H. (1991): An outline of Early Proterozoic crustal evolution in the Sao Francisco craton, Brazil: a review. *Precambrian Res.*, **53**, 1–22.
- Tucker, M. & Wright, P. (1999): “Carbonate sedimentology”. Blackwell Science ed., London, 330 p.
- Tudryn, A. & Tucholka, P. (2004): Magnetic monitoring of thermal alteration for natural pyrite and greigite. *Acta Geol. Pol.*, **52**, 509–520.
- Wasilewski, P. (1973): Magnetic hysteresis in natural materials. *Earth Planet. Sci. Lett.*, **20**, 67–72.
- Wirth, R. (2004): Focused Ion Beam (FIB) a novel technology for advanced application of micro- and nanoanalysis in geosciences and applied mineralogy. *Eur. J. Mineral.*, **16**, 863–876.

Received 27 May 2016

Modified version received 7 March 2017

Accepted 16 June 2017